JACS
JOURNAL OF THE AMERICAN CHEMICAL SOCIETY
Article
pubs.acs.org/JACS

Coexistence of High-T_c Ferromagnetism and *n*-Type Electrical Conductivity in $FeBi_2Se_4$

Kulugammana G. S. Ranmohotti,[†,⊥] Honore Djieutedjeu,[†,⊥] Juan Lopez,[†] Alexander Page,[‡] Neel Haldolaarachchige,[§] Hang Chi,[‡] Pranati Sahoo,[†] Ctirad Uher,[‡] David Young,[§] and Pierre F. P. Poudeu*[,†]

[†]Laboratory for Emerging Energy and Electronic Materials, Department of Materials Science and Engineering, University of Michigan, Ann Arbor, Michigan 48109, United States

[‡]Department of Physics, University of Michigan, Ann Arbor, Michigan 48109, United States

[§]Department of Physics and Astronomy, Louisiana State University, Baton Rouge, Louisiana 70803-4001, United States

Supporting Information

ABSTRACT: The discovery of *n*-type ferromagnetic semiconductors (*n*-FMSs) exhibiting high electrical conductivity and Curie temperature (T_c) above 300 K would dramatically improve semiconductor spintronics and pave the way for the fabrication of spin-based semiconducting devices. However, the realization of high-T_c *n*-FMSs and *p*-FMSs in conventional high-symmetry semiconductors has proven extremely difficult due to the strongly coupled and interacting magnetic and semiconducting sublattices. Here we show that decoupling the two functional sublattices in the low-symmetry semiconductor $FeBi_2Se_4$ enables unprecedented coexistence of high *n*-type electrical conduction and ferromagnetism with $T_c \approx 450$ K. The structure of $FeBi_2Se_4$ consists of well-ordered magnetic sublattices built of $[Fe_nSe_{4n+2}]_\infty$ single-chain edge-sharing octahedra, coherently embedded within the three-dimensional Bi-rich semiconducting framework. Magnetotransport data reveal a negative magnetoresistance, indicating spin-polarization of itinerant conducting electrons. These findings demonstrate that decoupling magnetic and semiconducting sublattices allows access to high-T_c *n*- and *p*-FMSs as well as helps unveil the mechanism of carrier-mediated ferromagnetism in spintronic materials.

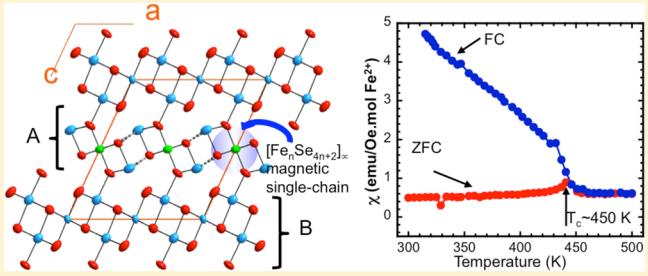

INTRODUCTION

Semiconductors exhibiting ferromagnetism and high electrical conduction above 300 K are of tremendous importance for the fabrication of practical spintronic devices.[1] Although these properties are accessible in metallic ferromagnets such as iron, cobalt, and nickel, the magnetic and conducting sublattices in such materials strongly interact, making it difficult to independently optimize the magnetic and semiconducting functionalities. However, the ability to independently control and manipulate ferromagnetism or electrical conduction within the material using external stimuli (electrical or magnetic field) is necessary for applications such as giant magnetoresistance memories, field sensors, spin transistors, and quantum information processing.[2−5] Therefore, ferromagnetic semiconductors (FMSs) have attracted tremendous attention due to the ability to tune their electrical conductivity via substitution chemistry and doping. The most popular approach to create FMSs involves substituting non-magnetic atoms in conventional semiconductors by magnetic atoms in order to generate the so-called diluted magnetic semiconductors (DMSs).[6−11] Most studied DMSs are *p*-type III−V and II−VI semiconductors in which the III or II atoms are partially substituted by Mn. In these materials, Mn atoms serve both as acceptors (providing holes) and as the magnetically active species (providing localized magnetic moments) in the semiconducting hosts. Therefore, the insertion of Mn atoms in these systems simultaneously alters the density of free carriers (holes) responsible for the electrical conduction and the concentration of localized spins (Mn^{2+}, 3d) responsible for the ferromagnetism. In addition, the Mn atoms in these systems are randomly distributed in the crystal lattice and occasionally enter into interstitial sites rather than occupying the crystallographic positions of the substituted atoms.[12−14] The inability to independently control (a) the effective concentration of Mn atoms, (b) the carrier density, and (c) the Mn−Mn separation in Mn-doped III−V and II−VI semiconductors has limited the Curie temperatures (T_c) of *p*-type dilute magnetic semiconductors (*p*-DMSs) to 185 K in $Ga_{1-x}Mn_xAs$, despite tremendous efforts to reach T_c above 300 K.[3,15,16] *p*-DMSs obtained via Mn substitution in group IV semiconductors (Si, Ge, SiGe) have also been investigated. Considerably larger ordering temperatures up to 400 K have been observed, for instance, in $Ge_{1-x}Mn_x$ films.[2,17,18] In these systems, the

Received: August 22, 2014
Published: December 24, 2014

DOI: 10.1021/ja5084255
J. Am. Chem. Soc. 2015, 137, 691−698

incorporation of Mn induced the formation of small Mn-rich precipitates (2−6 nm in diameter) randomly dispersed within the Mn-doped group IV semiconducting matrix. These precipitates are believed to be responsible for the high ordering temperature of the resulting $Ge_{1-x}Mn_x$ films.

Compared with the large volume of work on *p*-DMSs, *n*-type ferromagnetic semiconductors (*n*-FMSs) are poorly studied. However, *n*-FMSs are particularly interesting for semiconductor spintronics due to the high mobility of electrons and their remarkably long spin lifetimes in conventional semiconductors such as Si, GaAs, etc.[19−21] *n*-Type semiconducting behavior has been observed in FMSs such as $(In_{1-x}Fe_x)As$,[22] TiO_2,[23] $CdMnGeP_2$,[24] and $CdCr_2Se_4$.[25] These *n*-FMSs exhibit low Curie ordering temperatures, with the highest ordering temperature, $T_c \approx 132$ K, observed for the seleno-spinel $CdCr_2Se_4$.[25] Although $CdCr_2Se_4$ is not a conventional device material, its ability to grow epitaxially on conventional semiconductors such as GaAs to form $CdCr_2Se_4$/GaAs heterostructures has been demonstrated.[21] Furthermore, electrical injection of spin-polarized electrons from the *n*-FMS $CdCr_2Se_4$ into the GaAs-based device heterostructure was successfully realized.[21] This important result suggests that, beyond Mn-doped III−V, II−VI, and IV semiconductors, high-T_c *n*- and *p*-FMSs from other material systems that can be grown on conventional device substrates are very attractive for semiconductor spintronics.

Over the past 5 years, we have explored various strategies for the rational design and discovery of new high-T_c FMS structures encompassing ordered arrays of the magnetic atoms embedded within the semiconducting network of non-magnetic atoms. Our approach focuses on crystal engineering of the atomic structure of low-symmetry semiconducting main-group metal chalcogenides through chemical substitution of magnetic transition-metal atoms at targeted non-magnetic atomic positions. The structural and compositional flexibility of the resulting low-symmetry magnetic semiconducting transition-metal chalcogenides enables access to a large variety of electronic and magnetic properties through careful solid solution and doping studies.[26−33] For example, we have recently identified the fascinating class of ternary magnetic semiconductors, MPn_2Se_4 (M = Fe, Mn; Pn = Sb, Bi). The compounds are isostructural, crystallizing in the monoclinic space group $C2/m$ (No. 12). The crystal structure (Figure 1) can be divided into two types of building units, denoted A and B, alternating along [001]. Unit A is built of paired rods of face-sharing monocapped trigonal prisms alternating along the *a*-axis, with a $[M_nSe_{4n+2}]$ single chain of edge-sharing octahedra running parallel to [010]. Building unit B is a NaCl-type layer separating adjacent units A. The distribution of M and Pn atoms in the crystal structure is such that the $[M_nSe_{4n+2}]$ single chain within unit A is exclusively occupied by transition-metal atoms (M = Mn or Fe), whereas various degrees of mixed occupancy between Pn and M atoms are observed in the remaining metal positions. Despite the close similarity between their crystal structure, the dominant magnetic ordering in various compositions depends strongly on the nature of the magnetic atom (Mn, Fe) within the $[M_nSe_{4n+2}]$ chains (*magnetic subunit*). For instance, antiferromagnetic (AFM) ordering was observed in $MnSb_2Se_4$,[28] whereas $FeSb_2Se_4$ showed ferromagnetic (FM) behavior with a Curie transition temperature above 300 K.[27] Interestingly, the dominant charge carrier type (electrons or holes) in MPn_2Se_4 can be manipulated by altering the nature of the Pn atom within the

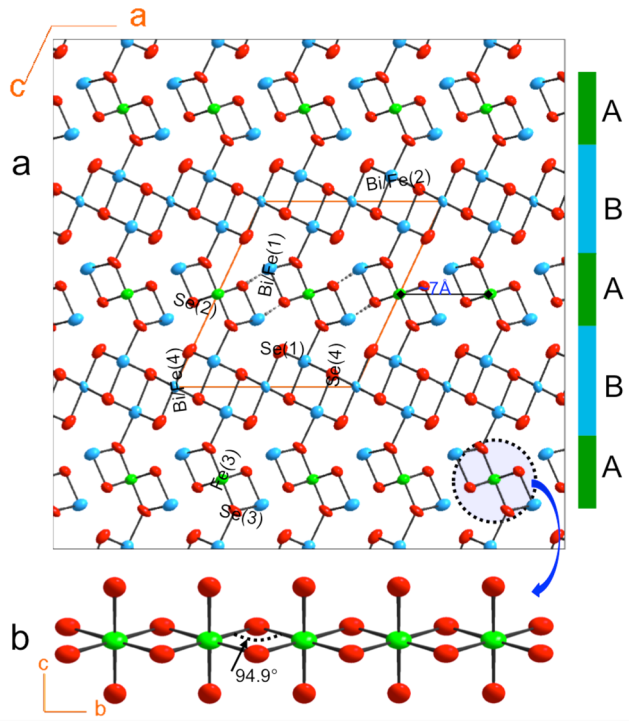

Figure 1. Crystal structure of $FeBi_2Se_4$ at 300 K. (a) Projection of the crystal structure along [010]. The building layers A and B alternating along the *c*-axis are highlighted. Ellipsoids are set at 98% probability for all atoms. Broken lines indicate (Bi/Fe)−Se interactions longer than 3.13 Å. (b) Structure of the magnetic sublattice featuring the 1D $[Fe(3)]_nSe_{4n+2}$ straight chain of edge-sharing $FeSe_6$ octahedra.

network (*semiconducting subunit*) separating adjacent $[M_nSe_{4n+2}]$ chains. For example, *p*-type semiconducting behavior was observed in $MnSb_2Se_4$[28] and $FeSb_2Se_4$,[27] whereas the bismuth analogue $MnBi_2Se_4$ exhibits *n*-type semiconductivity.[33] This ability to independently control the dominant magnetic ordering and carrier type within the crystal lattice of MPn_2Se_4 through chemical manipulation of the composition of various structural subunits makes it possible to create both *n*-type and *p*-type MPn_2Se_4 FMSs. Here, we report high-T_c ferromagnetism and large *n*-type electrical conductivity in $FeBi_2Se_4$, the bismuth analogue of the high-T_c *p*-type ferromagnet $FeSb_2Se_4$.[27] Magnetic susceptibility data from 2 to 600 K confirm FM ordering in $FeBi_2Se_4$, with a Curie temperature $T_c \approx 450$ K. Electronic charge transport (thermopower and electrical conductivity) and Hall-effect data indicate that $FeBi_2Se_4$ is an *n*-type degenerate semiconductor. Magnetoresistance data at 130 K reveal the presence of spin-polarized electrons, suggesting that $FeBi_2Se_4$ is a promising candidate for spintronic applications.

EXPERIMENTAL SECTION

Synthesis. $FeBi_2Se_4$ was synthesized as a single phase using high-purity Fe metal powder (CERAC, 99+%), Bi metal powder (ACROS, 99.5%), and Se powder (STREM, 99.99%) as starting materials. Because of the toxicity of elemental Se and its potentially explosive reaction with elemental Bi and Fe, great caution is advised during the synthesis procedure. The stoichiometric mixture of iron, bismuth, and selenium were thoroughly mixed under an argon atmosphere in a dry glovebox using an agate mortar with pestle and sealed in an evacuated quartz tube with a residual pressure of $\sim 10^{-3}$ Torr. The sealed tube was then placed in a furnace, and the temperature was initially ramped to 573 K in 12 h and held for 24 h. This first step is necessary to allow

DOI: 10.1021/ja5084255
J. Am. Chem. Soc. 2015, 137, 691−698

a non-explosive reaction between molten Se and Bi and Fe powder. The furnace temperature was then increased to 750 K in 12 h and held for 72 h, and finally cooled to room temperature over 24 h. To improve the crystallinity of the final product, the as-synthesized material was ground and reheated at 775 K for 5 days in an evacuated quartz tube. The resulting product was a polycrystalline dark gray powder. Single crystals suitable for crystal structure determination were grown by annealing the polycrystalline powder of $FeBi_2Se_4$ at 915 K for 9 days in an evacuated quartz tube. This annealing temperature was derived from the differential scanning calorimetry (DSC) of $FeBi_2Se_4$ (Figure S1). The synthesized air-stable polycrystalline powder of $FeBi_2Se_4$ was finely ground and used for further characterization. Approximately 3 g of the material was used for the fabrication of a high-density pellet for electronic transport and magnetoresistance measurements. The pellet was obtained by consolidating $FeBi_2Se_4$ powder at 673 K under an applied pressure of 100 MPa using a uniaxial hot press system. The relative density of the pressed pellet was above 98%. Detailed densification procedures are described elsewhere.[34−36] The resulting disk-shaped pellet with approximate thickness of 3 mm and diameter of 13 mm was polished, and rectangular bar specimens with various dimensions were cut from the disk using a precision wire saw (South Bay Technology). The rectangular bar samples were used for simultaneous measurement of the electrical conductivity and thermopower at high temperatures, magnetoresistance, and electrical conductivity at low temperatures.

Characterization. *X-ray Diffraction (XRD).* The XRD pattern of the synthesized $FeBi_2Se_4$ polycrystalline powder was recorded on a rotating anode Rigaku powder diffractometer operating under 40 kV and 40 mA using a monochromated Cu Kα radiation (λ = 1.5418 Å). X-ray data were collected in the 2θ range of 5−60° using a step-scanning mode with a 0.02° step width and 10 s count time. Good agreement (Figure S2) between the experimental XRD pattern and the theoretical pattern simulated using single-crystal structure data indicates the single-phase nature of the synthesized material.

Differential Scanning Calorimetry (DSC). The DSC measurement was performed on finely ground powder of the synthesized $FeBi_2Se_4$ material in order to confirm the phase purity and also to determine the melting and crystallization temperatures. DSC data were recorded using approximately 20 mg of the synthesized material and an equivalent mass of alumina (Al_2O_3) as the reference. Both the sample and the reference, sealed in a small quartz tube under a residual pressure of 10^{-3} Torr, were placed on the sample and reference pans of a F401 DSC apparatus (NETZSCH). The sample and reference were simultaneously heated under flowing nitrogen gas to 1073 K at a rate of 20 K/min, isothermed for 2 min, and then cooled to 300 K at a rate of 20 K/min. DSC data were recorded in two successive heating and cooling cycles. The endothermic onset temperatures are reported as the melting or crystallization points (Figure S1).

Crystal Structure Determination. A needle-shaped single crystal of $FeBi_2Se_4$ with dimensions 0.05 × 0.06 × 0.15 mm was used for X-ray data collection. Intensity data were recorded at 100, 300, and 400 K on a STOE imaging plate diffraction system (IPDS-2T) equipped with a low temperature attachment (Cryostream-700 from Oxford Cryosystems). Intensity data were indexed in the monoclinic crystal system, and the structure was solved by direct methods in the space group *C*2/*m* (No. 12) using the SHELTXL software package.[37] The structure solution revealed four crystallographically independent metal positions, M1 to M4, and four selenium positions, Se1 to Se4, within the asymmetric unit cell. In the first refinement cycle, Bi atoms were assigned to the general positions M1(4*i*) and M2(4*i*) located in a square pyramidal and octahedral coordination, respectively, while Fe atoms were located in the octahedrally coordinated special positions M3(2*c*) and M4(2*a*). The refinement of this model using full-matrix least-squares techniques resulted in reasonable thermal parameters for all atoms except Fe(4), which displayed a smaller thermal parameter compared to those of the Bi atoms. This suggested Fe/Bi mixed occupancy at the Fe(4) position. The refinement of this model resulted in more uniform thermal parameters for all atoms, and *R*1 dramatically dropped to 6%. However, the final composition showed excess positive charges. To search for a charge-balanced formula of the compound, Bi/Fe mixed occupancy at M1 and M2 positions was also considered. The refinement of this model resulted in an almost neutral composition with ∼16% Fe, ∼14% Fe, and ∼39% Fe in M1, M2, and M4 sites, respectively, while the M3 position remained fully occupied by Fe. In the final refinement step, an electroneutrality restraint was included along with secondary extinction correction and anisotropic displacement parameters for all atoms. The occupancy factors at M1, M2, and M4 positions were refined to the final values of M1 = 85%Bi + 15%Fe, M2 = 85%Bi + 15%Fe, and M4 = 60%Bi + 40%Fe, leading to a charge balanced formula of $FeBi_2Se_4$ assuming 2+, 3+, and 2− oxidation states for Fe, Bi, and Se, respectively. Crystallographic data for $FeBi_2Se_4$ at 100, 300, and 400 K are summarized in Table 1. The

Table 1. Selected Crystallographic Data and Details of Structure Determinations for $FeBi_2Se_4$ at 100, 300, and 400 K

parameter	data at 100 K | 300 K | 400 K
formula	$FeBi_2Se_4$
crystal system	monoclinic
space group	*C*2/*m* (No. 12)
formula weight (g/mol)	789.65
density (ρ_{cal}) (g/cm^3)	7.05 | 6.99 | 6.96
lattice parameters	
a (Å)	13.297(2) | 13.353(2) | 13.372(2)
b (Å)	4.1037(3) | 4.1171(3) | 4.1277(4)
c (Å)	15.038(3) | 15.069(3) | 15.072(2)
β (deg)	114.93(1) | 115.04(1) | 115.05(1)
volume (Å^3); *Z*	744.1(2) | 750.6(2) | 753.7(2); 4
crystal size (mm)	0.05 × 0.06 × 0.15
crystal shape, color	needle, black
diffractometer; radiation (Å)	IPDS-2T (Stoe); λ(Mo Kα) = 0.71073
ω range; $\Delta\omega$°; $2\theta_{max}$	180; 1; 58.5°
index range	$-18 \le h \le 18$; $-5 \le k \le 5$; $-20 \le l \le 20$
measured reflections	6609 | 4131 | 4341
unique reflections	1140| 1147 | 1149
R_{int}	0.078 | 0.120 | 0.1153
R_σ	0.040 | 0.093 | 0.078
μ (cm^{-1})	685 | 680 | 676
no. of parameters	49
extinction correction, *x*	0.00141(1) | 0.00166(1) | 0.00195(1)
difference electron density (e/Å^3)	+2.18 to −2.51 | +2.96 to −1.71 | +2.30 to −2.14
$R_1(F_o > 4\sigma(F_o))^a$	0.027 | 0.038 | 0.037
wR_2 (all)^b	0.064 | 0.086 | 0.077
GooF	1.070 | 1.061 | 1.112

$^aR_1 = \sum||F_o| - |F_c||/\sum|F_o|$. $^bwR_2 = [\sum w(F_o^2 - F_c^2)^2/\sum w(F_o^2)^2]^{1/2}$.

atomic coordinates and isotropic displacement parameters of all atoms are given in Table 2. Selected interatomic bond distances in $FeBi_2Se_4$ are compared in Table 3. The software Diamond was utilized to create the graphic representation of the crystal structure with ellipsoid representations (98% probability level) for all atoms.[38] Changes in the lattice parameters of the $FeBi_2Se_4$ single crystal upon warming from 100 to 400 K are given in Table S1. Further details of the crystal structure investigation are given in CIF format as Supporting Information and can also be obtained from the Fachinformationszentrum Karlsruhe, 76344 Eggenstein- Leopoldshafen, Germany, (fax: +49 7247 808 666; e-mail: crysdata@fiz.karlsruhe.de) on quoting the depository numbers CSD_427627 for $FeBi_2Se_4$ at 100 K, CSD_427628 for $FeBi_2Se_4$ at 300 K, and CSD_427629 for $FeBi_2Se_4$ at 400 K.

Magnetic Measurements. Magnetic susceptibility measurements were performed on polycrystalline powder of $FeBi_2Se_4$ (32.6 mg) using a Quantum Design MPMS-XL SQUID magnetometer. Direct current (dc) field-cooled (FC) and zero-field-cooled (ZFC) magnetic

DOI: 10.1021/ja5084255
J. Am. Chem. Soc. 2015, 137, 691−698

Table 2. Wyckoff Positions, Site Occupancy Factors (k), Atomic Coordinates, and Equivalent Isotropic Displacement Parameters (U_{eq}/pm^2) for All Atoms in the Asymmetric Unit of $FeBi_2Se_4$ at 400 K | 300 K | 100 K[a]

atom	Wyck.	k	x	y	z	U_{eq}[b]
Bi1	4i	0.85(1)	0.2177(1)	0	0.3625(1)	376
			0.2177(1)		0.3626(1)	240
			0.2174(1)		0.3623(1)	130
Fe1	4i	0.15(1)	0.2177(1)	0	0.3625(1)	376
			0.2177(1)		0.3626(1)	240
			0.2174(1)		0.3623(1)	130
Bi2	4i	0.85(1)	0.3494(1)	1/2	0.1374(1)	315
			0.3494(1)		0.1371(1)	199
			0.3494(1)		0.1367(1)	115
Fe2	4i	0.15(1)	0.3494(1)	1/2	0.1374(1)	315
			0.3494(1)		0.1371(1)	199
			0.3494(1)		0.1367(1)	115
Fe3	2c		1/2	1/2	1/2	385
						216
						98
Bi4	2b	0.60(1)	1/2	0	0	257
						138
						67
Fe4	2b	0.40(1)	1/2	0	0	257
						138
						67
Se1	4i		0.5091(2)	0	0.1930(2)	257
			0.5091(2)		0.1929(2)	245
			0.5094(2)		0.1930(2)	168
Se2	4i		0.1138(2)	1/2	0.4559(1)	329
			0.1136(2)		0.4564(2)	199
			0.1132(2)		0.4565(2)	130
Se3	4i		0.3466(2)	1/2	0.3299(2)	328
			0.3469(2)		0.3298(2)	215
			0.3462(2)		0.3295(2)	141
Se4	4i		0.1635(2)	0	0.0670(1)	322
			0.1638(2)		0.0665(2)	211
			0.1635(2)		0.0663(2)	133

[a]Estimated standard deviations corresponding to the last digits are indicated in parentheses. [b]U_{eq} is defined as one-third of the trace of the orthogonalized U_{ij} tensor.

susceptibility measurements were performed over a temperature range from 5 to 300 K using an applied field of 100 Oe. The sample was first ZFC to 5 K, and the measurement was performed on heating. For the FC measurements, a 100 Oe magnetic field was applied upon cooling to 5 K. High-temperature magnetic susceptibility data were measured from 300 to 500 K under an applied field of 100 Oe. The sample was initially heated to 500 K and cooled to 300 K under an applied field of 100 Oe. The FC susceptibility curve was then recorded during the second heating run. The sample was subsequently cooled to 300 K under zero-field, and the ZFC susceptibility data were collected during the third heating run. Isothermal magnetization measurements were carried out at 300, 400, 450, and 500 K in a dc magnetic field varying from 0 to ±3000 Oe.

Heat Capacity (C_p). Heat capacity was measured from 10 to 160 K under zero applied field using a Quantum Design Physical Property Measurement System (PPMS). C_p data were recorded using approximately 25 mg of the synthesized material. For accurate determination of the heat capacity, the addenda measurement, which records the heat capacity of the grease (used for thermal contact) and the platform, was subtracted from the heat capacity obtained from the measurement of sample, grease, and platform.

Electrical Transport Properties. Low-temperature electrical conductivity was measured from 3 to 300 K on a rectangular bar sample using a standard four-probe method in a PPMS. Thermopower and electrical conductivity data from 300 to 575 K were measured simultaneously on a 2.5 mm × 2.5 mm × 10 mm rectangular bar specimen using a commercial ZEM-3 Seebeck coefficient/electrical resistivity measurement system (ULVAC-RIKO, Japan). To ensure reproducibility, data were collected on three heating and cooling cycles under a residual pressure of He gas. The instrument precision on the electrical conductivity and thermopower data is ±4%.

Hall Effect. The Hall coefficients were measured in the temperature range from 300 to 823 K under the magnetic field of 1T using a custom-made apparatus consisting of a large Oxford air-bore superconducting magnet cryostat that accommodates a small tubular oven and a Hall insert. The instrument uncertainty on Hall coefficient data is ±5%. The electrical conductivity data were combined with the Hall coefficient measurement to evaluate and extract accurate information on the temperature dependence of the carrier density and the mobility of the charge carriers in $FeBi_2Se_4$.

Magnetoresistance. The magnetoresistance was measured in the PPMS at 130 K on a 1 mm × 1 mm × 6 mm rectangular bar sample cut from the hot-pressed pellet. The applied field was varied between 0 and 40 kOe.

Table 3. Selected Interatomic Distances (Å) in $FeBi_2Se_4$ at Different Temperatures[a]

bond	400 K	300 K	100 K	% contraction
Bi1|Fe1—Se2^{i}	2.710(3)	2.704(3)	2.706(2)	**+0.07**
Bi1|Fe1—Se(3,3^{ii})	2.862(2)	2.860(2)	2.846(2)	−0.50
Bi1|Fe1—Se(2,2^{ii})	3.134(2)	3.135(2)	3.129(2)	−0.19
Bi2|Fe2—Se(1,1^{v})	2.830(2)	2.823(2)	2.817(2)	−0.21
Bi2|Fe2—Se3	2.917(3)	2.917(3)	2.918(2)	**+0.03**
Bi2|Fe2—Se4^{vi}	3.013(3)	2.998(3)	2.983(2)	−0.50
Bi2|Fe2—Se(4,4^{v})	3.055(2)	3.047(2)	3.039(2)	−0.26
Fe3—Se(3,3^{vii})	2.516(3)	2.514(3)	2.518(2)	**+0.16**
Fe3—Se2$^{(i,viii,ix,x)}$	2.806(2)	2.796(2)	2.781(2)	−0.54
ν_1	0.90	0.90	0.91	
Bi4|Fe4—Se(1,1^{xii})	2.859(3)	2.857(3)	2.851(2)	−0.21
Bi4|Fe4—Se(4^{xi,viii,vi,ix})	2.862(2)	2.858(2)	2.847(2)	−0.38
ν_2	0.99	1.00	1.00	

[a]Standard deviations corresponding to the last digits are indicated in parentheses. ν = (apical bond length)/(equatorial bond length). Operators for generating equivalent atoms: (i) $^1/_2 - x, ^1/_2 - y, 1 - z$; (ii) $x, -1 + y, z$; (iii) $-^1/_2 + x, -^1/_2 + y, z$; (iv) $-^1/_2 + x, ^1/_2 + y, z$; (v) $x, 1 + y, z$; (vi) $^1/_2 - x, ^1/_2 - y, -z$; (vii) $1 - x, 1 - y, 1 - z$; (viii) $^1/_2 + x, ^1/_2 + y, z$; (ix) $^1/_2 + x, -^1/_2 + y, z$; (x) $^1/_2 - x, ^3/_2 - y, 1 - z$; (xi) $^1/_2 - x, -^1/_2 - y, -z$; (xii) $1 - x, -y, -z$.

DOI: 10.1021/ja5084255
J. Am. Chem. Soc. 2015, 137, 691−698

RESULTS AND DISCUSSION

Synthesis and Structure. Polycrystalline powder of $FeBi_2Se_4$ was synthesized by solid-state reaction of high-purity elements at 750 K for 72 h. Single crystals, suitable for X-ray structure determination, were grown by annealing the as-synthesized polycrystalline powder of $FeBi_2Se_4$ at 915 K for 9 days. Careful analysis of single-crystal X-ray diffraction data at 300 K indicates that $FeBi_2Se_4$ (Table 1) is isostructural with $FeSb_2Se_4$,[27] crystallizing in the monoclinic space group $C2/m$ (No. 12) with lattice parameters a = 13.353(2) Å, b = 4.1171(3) Å, c = 15.069(3) Å, β = 115.04(3)°, and V = 750.6(2) Å^3. It is interesting to note that, despite the large difference ($\Delta R/R \approx 54\%$) in the effective ionic radii of Sb^{3+} (76 pm) and Bi^{3+} (117 pm) in octahedral coordination,[39] the complete substitution of antimony by bismuth in the structure of $FeSb_2Se_4$ maintains the overall symmetry of the original structure essentially unchanged with only marginal increase in the lattice parameters. This confirms the remarkable structural and compositional flexibility of the $FeSb_2Se_4$ structure type.

The structure of $FeBi_2Se_4$ can be divided into two types of layered units, denoted as A and B, parallel to ab planes and alternating along the c-axis (Figure 1). Four crystallographically independent metal positions, two general positions M1(4i) and M2(4i) and two special positions M3(2c) and M4(2a) (Table 2), were found in the crystal structure. The M1(4i) site is located in a [1+2+2] distorted square pyramidal geometry of Se atoms, whereas atoms at M2(4i), M3(2c), and M4(2a) positions are octahedrally coordinated by Se atoms (Table 3). Within layer A, the M1(4i) position is mixed occupied by 85% Bi + 15% Fe, whereas the M3 (2c) site is fully occupied by Fe. The flattened $Fe(3)Se_{[2+4]}$ octahedra (with two short axial bonds and four long equatorial bonds) share edges to form $[Fe(3)_nSe_{4n+2}]_\infty$ single chains (1D) running along the b-axis (Figure 1b). The intrachain Fe–Fe distance is 4.128(1) Å. Likewise, adjacent $[Bi/Fe(1)]Se_5$ square pyramids also share edges to form a double chain running along the b-axis and parallel to the $[Fe(3)_nSe_{4n+2}]_\infty$ single chains. Therefore, layer A can be described as consisting of a parallel arrangement of $[Fe(3)_nSe_{4n+2}]_\infty$ single chains along the a-axis separated by a double chain of edge-sharing $[Bi/Fe(1)]Se_5$ square pyramids. The distance between adjacent $[Fe(3)_nSe_{4n+2}]_\infty$ single chains within layer A is 6.996(1) Å, suggesting that they are magnetically isolated from each other. The M2(4i) and M4(2a) positions within layer B are mixed occupied by Bi and Fe atoms. While the M2 sites with distorted [2+1+1+2] octahedral coordination geometry contain 85% Bi + 15% Fe, the M4 position with nearly perfect octahedral geometry (Table 3) is occupied by 60% Bi + 40% Fe. Adjacent $[M2]Se_6$ and $[M4]Se_6$ octahedra share all edges to build a three-octahedra-thick NaCl-type layer denoted by B. Adjacent layers A and B are connected to each other through M1–Se3–M2 linkage to form a three-dimensional (3D) structure. The chemical composition obtained from the refinement of the distribution of Fe and Bi atoms in various metal positions within the crystal structure of $FeBi_2Se_4$ suggests that Fe, Bi, and Se exist in the 2+, 3+, and −2 oxidation states, respectively.

Magnetism. To evaluate the magnetic behavior of $FeBi_2Se_4$, temperature dependent magnetic susceptibility measurements were carried out from 2 to 600 K under an applied field of 100 Oe using a superconducting quantum interference device (SQUID) magnetometer. The large room temperature value of the magnetic susceptibility, 5 emu/Oe·mol Fe^{2+}, indicates a FM behavior for $FeBi_2Se_4$ with T_c > 300 K. At low temperatures (T < 300 K), field-cooled (FC) and zero-field-cooled (ZFC) magnetic susceptibility (Figure 2a) overlap from ~125 to 300 K

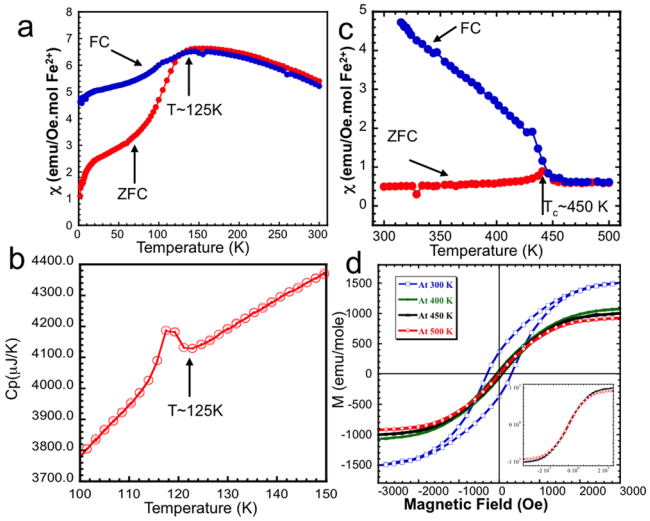

Figure 2. Magnetic properties and heat capacity of $FeBi_2Se_4$. (a) Low-temperature (T < 300 K) field-cooled (FC) and zero-field-cooled (ZFC) magnetic susceptibility measured under 100 Oe showing a magnetic transition at 125 K. (b) Temperature-dependent heat capacity, highlighting an anomalous increase in magnitude around the magnetic transition temperature. (c) High-temperature FC and ZFC magnetic susceptibility measured under 100 Oe, showing a Curie transition temperature at ~450 K. (d) Magnetization loops below (300 and 400 K) and above (450 and 500 K) the Curie transition temperature. Coercive fields of 300 and 110 Oe were observed at 300 and 400 K, respectively, while a very low coercive field is observed at 450 K and above (inset).

and gradually increase with decreasing temperature. A sharp drop in the susceptibility and a divergence of the ZFC and FC curves are observed with further cooling below 125 K. An anomalous increase in magnitude of the heat capacity (C_p) was also observed around the magnetic transition (Figure 2b). This suggests that the magnetic transition is of first-order and presumably results from a structural transition below 125 K. To further investigate the origin of such a transition, we analyzed changes in the unit cell parameters (Table S1) and the crystal structure (Figure S3) of $FeBi_2Se_4$ as the single crystal was cooled from 400 to 100 K. A plot of the relative change in the lattice parameters ($\Delta L/L$) as a function of temperature (Figure S1) indicates a preferential contraction of a and b parameters, whereas contraction along the c-axis is marginal. This results in a small distortion of the $Fe(3)Se_{[2+4]}$ octahedra within layer A. At 100 K, the apical Fe(3)–Se bonds expand by 0.16%, whereas the equatorial bonds contract by 0.54% (Supplementary Table 3). Such small alteration in the geometry of edge-sharing octahedra building the $[Fe(3)_nSe_{4n+2}]_\infty$ single magnetic chains changes the distribution of spins within the $3d^6$ orbital of Fe^{2+}, which in turn affect the magnetic susceptibility of $FeBi_2Se_4$ below 125 K. However, the FM behavior of the compound is maintained below 125 K. A similar magnetic transition was observed in the susceptibility curves of $FeSb_2Se_4$.[27] The FC magnetic susceptibility of $FeBi_2Se_4$ above 300 K gradually decreases with rising temperature up to 450 K, at which point a sharp drop in the susceptibility is observed (Figure 2c). Thereafter, the susceptibility remains constant with

DOI: 10.1021/ja5084255
J. Am. Chem. Soc. 2015, 137, 691–698

further increase in the temperature. This indicates that the FM behavior of $FeBi_2Se_4$ persists up to $T_c \approx 450$ K, above which a superparamagnetic behavior is observed. Surprisingly, the ZFC curve measured after cooling the sample from 500 to 300 K without applied external field starts with a lower susceptibility value (~0.5 emu/Oe mol) compared to the ZFC susceptibility value at 300 K from the low-temperature data. This indicates that after heating the sample above T_c (~500 K) the spins of a large fraction of free carriers contributing to the magnetism are randomized. This random alignment of spins is maintained upon cooling at 300 K under zero-applied field leading to lower susceptibility values. This discrepancy between ZFC data at low temperature and high temperature suggests that spins of free carriers are coupled to localized magnetic moments and largely contribute to the magnetism in $FeBi_2Se_4$.

Field-dependent magnetization loops at 300 and 400 K (Figure 2d) show the characteristic S-shape of a ferromagnet with a coercive field of 300 and 110 Oe, respectively, while a very low coercive field is observed at 450 K and above. This is consistent with the FM ordering up to 450 K. Interestingly, the magnetization does not reach saturation suggesting a large degree of spin disorder with a high magnetic anisotropy, which may arise from the 1D structure of the $[Fe(3)_nSe_{4n+2}]_\infty$ single magnetic chains. Taking into account the large intralayer distance of ~7 Å and the interlayer separation of ~15 Å between $[Fe(3)_nSe_{4n+2}]_\infty$ magnetic chains within the crystal structure of $FeBi_2Se_4$, we attribute the high-T_c FM behavior to a combination of weak FM interactions between adjacent Fe atoms within individual $[Fe(3)_nSe_{4n+2}]_\infty$ magnetic chain and long-range coupling of localized intrachain moments via formation of overlapping bound magnetic polarons (BMPs) and/or carrier-mediated mechanisms.

The flattened shape of the $[Fe(3)]Se_{2+4}$ octahedra within the magnetic chains, induces a high-spin distribution of $3d^6$ electrons leading to a total spin value of $S = 2$. The intrachain magnetic interaction between adjacent Fe atoms, 4.128 Å apart, is likely achieved by indirect exchange interaction through the bridging Se(2) atom (Figure 1b). The Fe(3)−Se(2)−Fe(3) bond angle of 94.9° suggests weak FM coupling of adjacent Fe atoms within $[Fe(3)_nSe_{4n+2}]_\infty$ single magnetic chains.[40−42] This implies a non-zero localized magnetic moment for individual $[Fe(3)_nSe_{4n+2}]_\infty$ chains. The remaining metal sites (M1, M2, and M4) in the crystal structure contain various amounts of Fe mixed with Bi atoms. Therefore, each Bi/Fe metal position within the semiconducting network separating adjacent $[Fe(3)_nSe_{4n+2}]_\infty$ chains is a potential site for the nucleation of BMPs due to the interaction of itinerant electrons and localized Fe ($3d^6$) spins.[43,44] The interaction of BMPs with the localized moment of $[Fe(3)_nSe_{4n+2}]_\infty$ chains within their orbits enables FM coupling on neighboring $[Fe(3)_nSe_{4n+2}]_\infty$ chains falling within the orbit of the same BMP. Because of the short separation between Bi/Fe sites in the crystal structure, the formation of a high density of overlapping BMPs can be anticipated throughout the semiconducting network. Therefore, long-range FM ordering of localized $[Fe(3)_nSe_{4n+2}]_\infty$ moments in the crystal structure can be established. Evidence of a significant contribution of BMPs to the FM ordering in $FeBi_2Se_4$ is provided by the large values of magnetic susceptibility, as well as the S-shape of the magnetization loop above T_c. Neutron experiments to further probe the magnetic structure of this compound are in progress.

Electronic Properties. The most interesting observation is the coexistence in $FeBi_2Se_4$ of high-T_c ferromagnetism with *n*-type conductivity. The electrical conductivity at zero-field (Figure 3a) gradually decreases with rising temperature, from

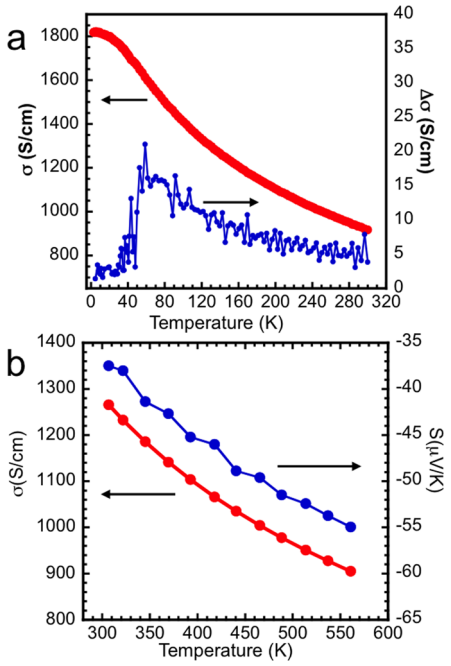

Figure 3. Electrical properties of $FeBi_2Se_4$ as a function of temperature. (a) Electrical conductivity (σ, red symbols) and absolute variation in electrical conductivity ($\Delta\sigma$, blue symbols) below 300 K. A sharp increase in the slope is observed around 130 K. (b) Electrical conductivity (σ, red symbols) and thermopower (S, blue symbols) above 300 K.

~1800 S/cm at 2 K to 900 S/cm at 550 K, which is typical behavior for heavily doped semiconductors. The temperature dependent electrical conductivity data above 50 K are well fit by the power law $T^{-\alpha}$ as expected for acoustic phonon scattering of charge carriers.[45] Interestingly, the power exponent decreases from $\alpha \approx 0.54$ for electrical conductivity data at temperatures above 130 K to $\alpha \approx 0.26$ for data between 50 and 130 K. A plot of the absolute change in the electrical conductivity ($\Delta\sigma = \sigma(T + \Delta T) - \sigma(T)$) as a function of temperature (Figure 3a) also indicates an increase, around 130 K, of the rate of conductivity increase with decreasing temperature. The decrease in the power exponent is attributed to the above-described anisotropic lattice contraction upon cooling below 130 K (Figure S4). Within this temperature regime ($T < 130$ K), contraction of the Bi/Fe(1)−Se(2) bond below 3.13 Å results in the connectivity of the crystal structure of $FeBi_2Se_4$ into a three-dimensional network (Figure S3). This induces an increase in the electrical conductivity due to a decrease in the electrical band gap.

Hall effect measurements between 300 and 823 K reveal a negative Hall coefficient (R_H), indicating electrons as the majority charge carrier (Figure 4a). The *n*-type character of the electrical conduction in the high-T_c ferromagnet $FeBi_2Se_4$ is also supported by the negative values of the thermopower (Figure 3b). The thermopower increases with rising temperature from −37 μV/K at 300 K to −55 μV/K at 575 K. Carrier (electron) density extracted from the Hall effect measurement is 4×10^{19} cm^{-3} at 300 K and exponentially increases with rising temperature to 16×10^{19} cm^{-3} at 823 K (Figure 4b). This trend is consistent with the thermally activated behavior

DOI: 10.1021/ja5084255
J. Am. Chem. Soc. 2015, 137, 691−698

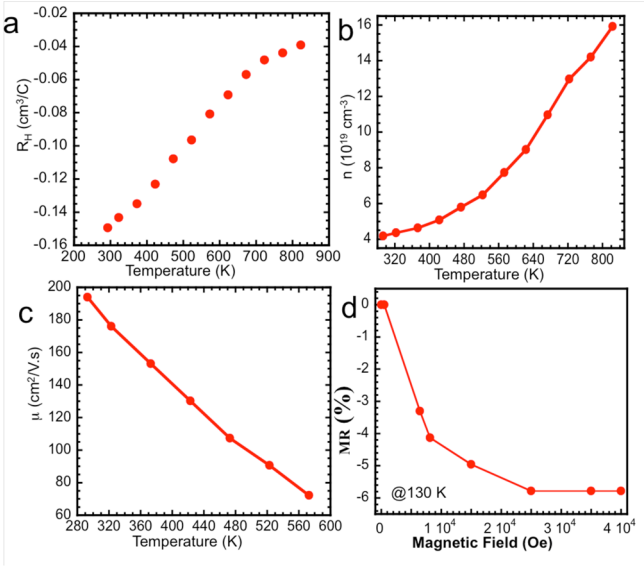

Figure 4. High-temperature electronic transport and magnetoresistance of $FeBi_2Se_4$: (a) Hall coefficient, (b) carrier concentration, (c) carrier mobility, and (d) magnetoresistance at 130 K.

expected in intrinsic semiconductors. Fitting of the high-temperature (T > 400 K) data using the exponential function $n(T) \approx \exp(-E_g/2k_BT)$ yields an electrical band gap, E_g = 0.24 eV. This confirms $FeBi_2Se_4$ as a narrow band gap n-FMS with T_c > 400 K.

Interestingly, high electron mobility, ~190 $cm^2/V{\cdot}s$ (Figure 4c), is observed at 300 K, which is a reasonable number for a doped FMS with a carrier density of ~10^{19} cm^{-3}. Also, the mobility decreases with rising temperature accordingly to the power law $\mu \approx T^{-\alpha}$, with α = 1.42, which is very close to the value of α = 1.5 expected for carrier transport dominated by acoustic phonon scattering.[45] These results are comparable with carrier transport in non-magnetic semiconductors, suggesting a weak electronic interaction, under zero-field, between free electrons in the semiconducting sublattice and localized spins in the magnetic sublattice of $FeBi_2Se_4$. However, the coexistence within the semiconducting sublattice of localized spins and a high density of free electrons with high mobility, arising from the intermixing of Bi and Fe at various metal positions, is favorable to the formation of spin-polarized itinerant electrons leading to overlapping BMPs, which are believed to be responsible for the large magnetic susceptibility and high T_c observed in $FeBi_2Se_4$.

$FeBi_2Se_4$ shows negative magnetoresistance (MR = $[\rho(H) - \rho(0)]/\rho(0)$, where $\rho(H)$ and $\rho(0)$ are the resistivity at a magnetic field H and 0, respectively) values (Figure 4d). This indicates a reduction in the scattering of free-electrons by localized spins due to the alignment of magnetic moments of Fe atoms and spins of free electrons parallel to the applied field (H). The MR at 130 K increases rapidly with rising field and reaches saturation at MR ≈ − 6% under an applied field of 25 kOe. The low value of the MR provides evidence for the presence of spin-polarized electrons within the semiconducting sublattice and their weak interaction with localized moments within the magnetic sublattice.

CONCLUDING REMARKS

In summary, we have demonstrated a new n-type semiconductor, $FeBi_2Se_4$, with high carrier mobility and high electrical conductivity, featuring ferromagnetic behavior up to T_c > 400 K. The unique combination of these two functionalities in $FeBi_2Se_4$ arises from the low-symmetry crystal structure of MPn_2Se_4, which enables the atomic-scale integration of two crystallographically independent magnetic and semiconducting sublattices. This allows independent alteration of the magnetic and/or the semiconducting behavior through the manipulation of the chemical composition of each sublattice. For instance, predominantly FM ordering is observed for M = Fe ($FePn_2Se_4$),[27] while M = Mn ($MnPn_2Se_4$) is predominantly AFM.[28,33] In addition, p-type electrical conductivity is obtained for Pn = Sb (MSb_2Se_4),[27] whereas Pn = Bi (MBi_2Se_4) exhibits n-type semiconducting behavior.[33] Therefore, by integrating Fe within the magnetic sublattice and Bi within the semiconducting lattice, we have successfully designed an n-FMS with T_c > 400 K and large electrical conductivity. To the best of our knowledge, this combination of large n-type conductivity and ferromagnetic behavior at high temperature achieved in $FeBi_2Se_4$ has never been observed in any other FMS. The importance of this result for the future of spintronic research is two-fold. First, it shows that by decoupling electronically and structurally the magnetic and semiconducting functionalities at the atomic scale, one can achieve both n- and p-FMSs with a high T_c. This should pave the way for the design and fabrication of spin-based semiconducting devices such as light-emitting diodes and field-effect transistors. Second, the ability to independently manipulate the chemistry of the semiconducting sublattice in the MPn_2Se_4 structure via substitution and/or doping without altering the chemistry of the magnetic sublattice can be exploited to study longstanding fundamental questions related to the mechanism of carrier-mediated ferromagnetism in spintronic materials.

ASSOCIATED CONTENT

Supporting Information

X-ray crystallographic data, in CIF format, for the single-crystal structure refinements of $FeBi_2Se_4$ at 100, 300, and 400 K; Table S1 and Figures S1−S4. This material is available free of charge via the Internet at http://pubs.acs.org.

AUTHOR INFORMATION

Corresponding Author

*ppoudeup@umich.edu

Author Contributions

⊥K.G.S.R. and H.D. contributed equally to this work.

Notes

The authors declare no competing financial interest.

ACKNOWLEDGMENTS

This work was supported by the National Science Foundation (NSF) Career Award DMR-1237550. C.U. and P.F.P.P. also gratefully acknowledge financial support from the U.S. Department of Energy, Office of Basic Energy Sciences, under Award No. DE-SC-0008574. D.P.Y. acknowledges support from the NSF under grant no. DMR-1306392. Magnetic data were recorded on a SQUID magnetometer at the University of Michigan purchased using an MRI grant from the NSF (CHE-104008).

DOI: 10.1021/ja5084255
J. Am. Chem. Soc. 2015, 137, 691−698

REFERENCES

(1) Wolf, S. A.; Awschalom, D. D.; Buhrman, R. A.; Daughton, J. M.; von Molnar, S.; Roukes, M. L.; Chtchelkanova, A. Y.; Treger, D. M. *Science* **2001**, *294*, 1488.
(2) Jamet, M.; Barski, A.; Devillers, T.; Poydenot, V.; Dujardin, R.; Bayle-Guillemaud, P.; Rothman, J.; Bellet-Amalric, E.; Marty, A.; Cibert, J.; Mattana, R.; Tatarenko, S. *Nat. Mater.* **2006**, *5*, 653.
(3) Macdonald, A. H.; Schiffer, P.; Samarth, N. *Nat. Mater.* **2005**, *4*, 195.
(4) Zutic, I.; Fabian, J.; Erwin, S. C. *IBM J. Res. Dev* **2006**, *50*, 121.
(5) Zutic, I.; Fabian, J.; Das Sarma, S. *Rev. Mod. Phys.* **2004**, *76*, 323.
(6) Dobrowolska, M.; Tivakornsasithorn, K.; Liu, X.; Furdyna, J. K.; Berciu, M.; Yu, K. M.; Walukiewicz, W. *Nat. Mater.* **2012**, *11*, 444.
(7) Richardella, A.; Roushan, P.; Mack, S.; Zhou, B.; Huse, D. A.; Awschalom, D. D.; Yazdani, A. *Science* **2010**, *327*, 665.
(8) Sawicki, M.; Chiba, D.; Korbecka, A.; Nishitani, Y.; Majewski, J. A.; Matsukura, F.; Dietl, T.; Ohno, H. *Nat. Phys.* **2010**, *6*, 22.
(9) Dietl, T.; Ohno, H.; Matsukura, F.; Cibert, J.; Ferrand, D. *Science* **2000**, *287*, 1019.
(10) Dietl, T. *Semicond. Sci. Technol.* **2002**, *17*, 377.
(11) Dietl, T. *Nat. Mater.* **2010**, *9*, 965.
(12) Edmonds, K. W.; Boguslawski, P.; Wang, K. Y.; Campion, R. P.; Novikov, S. N.; Farley, N. R. S.; Gallagher, B. L.; Foxon, C. T.; Sawicki, M.; Dietl, T.; Nardelli, M. B.; Bernholc, J. *Phys. Rev. Lett.* **2004**, *92*, 037201.
(13) Blinowski, J.; Kacman, P. *Phys. Rev. B* **2003**, *67*, 121204.
(14) Yu, K. M.; Walukiewicz, W.; Wojtowicz, T.; Kuryliszyn, I.; Liu, X.; Sasaki, Y.; Furdyna, J. K. *Phys. Rev. B* **2002**, *65*, 201303.
(15) Jungwirth, T.; Wang, K. Y.; Masek, J.; Edmonds, K. W.; Konig, J.; Sinova, J.; Polini, M.; Goncharuk, N. A.; MacDonald, A. H.; Sawicki, M.; Rushforth, A. W.; Campion, R. P.; Zhao, L. X.; Foxon, C. T.; Gallagher, B. L. *Phys. Rev. B* **2005**, *72*, 165204.
(16) Wang, M.; Campion, R. P.; Rushforth, A. W.; Edmonds, K. W.; Foxon, C. T.; Gallagher, B. L. *Appl. Phys. Lett.* **2008**, *93*, 132103.
(17) Park, Y. D.; Hanbicki, A. T.; Erwin, S. C.; Hellberg, C. S.; Sullivan, J. M.; Mattson, J. E.; Ambrose, T. F.; Wilson, A.; Spanos, G.; Jonker, B. T. *Science* **2002**, *295*, 651.
(18) Kang, J. S.; Kim, G.; Wi, S. C.; Lee, S. S.; Choi, S.; Cho, S.; Han, S. W.; Kim, K. H.; Song, H. J.; Shin, H. J.; Sekiyama, A.; Kasai, S.; Suga, S.; Min, B. I. *Phys. Rev. Lett.* **2005**, *94*, 147202.
(19) Oestreich, M. *Nature* **1999**, *402*, 735.
(20) Kikkawa, J. M.; Awschalom, D. D. *Nature* **1999**, *397*, 139.
(21) Kioseoglou, G.; Hanbicki, A. T.; Sullivan, J. M.; van't Erve, O. M. J.; Li, C. H.; Erwin, S. C.; Mallory, R.; Yasar, M.; Petrou, A.; Jonker, B. T. *Nat. Mater.* **2004**, *3*, 799.
(22) Hai, P. N.; Anh, L. D.; Tanaka, M. *Appl. Phys. Lett.* **2012**, *101*, 252410.
(23) Matsumoto, Y. *Science* **2001**, *294*, 1003.
(24) Medvedkin, G. A.; Ishibashi, T.; Nishi, T.; Hayata, K.; Hasegawa, Y.; Sato, K. *Jpn. J. Appl. Phys. 2* **2000**, *39*, L949.
(25) Sanford, N.; Davies, R. W.; Lempicki, A.; Miniscalco, W. J.; Nettel, S. J. *Phys. Rev. Lett.* **1983**, *50*, 1803.
(26) Anglin, C.; Takas, N.; Callejas, J.; Poudeu, P. F. P. *J. Solid State Chem.* **2010**, *183*, 1529.
(27) Djieutedjeu, H.; Poudeu, P. F. P.; Takas, N. J.; Makongo, J. P. A.; Rotaru, A.; Ranmohotti, K. G. S.; Anglin, C. J.; Spinu, L.; Wiley, J. B. *Angew. Chem., Int. Ed.* **2010**, *49*, 9977.
(28) Djieutedjeu, H.; Makongo, J. P. A.; Rotaru, A.; Palasyuk, A.; Takas, N. J.; Zhou, X. Y.; Ranmohotti, K. G. S.; Spinu, L.; Uher, C.; Poudeu, P. F. P. *Eur. J. Inorg. Chem.* **2011**, 3969.
(29) Matsushita, Y.; Ueda, Y. *Inorg. Chem.* **2003**, *42*, 7830.
(30) Mrotzek, A.; Kanatzidis, M. G. *Acc. Chem. Res.* **2003**, *36*, 111.
(31) Poudeu, P. F. P.; Takas, N.; Anglin, C.; Eastwood, J.; Rivera, A. *J. Am. Chem. Soc.* **2010**, *132*, 5751.
(32) Poudeu, P. F. P.; Djieutedjeu, H.; Sahoo, P. *Z. Anorg. Allg. Chem.* **2012**, *638*, 2549.
(33) Ranmohotti, K. G. S.; Djieutedjeu, H.; Poudeu, P. F. P. *J. Am. Chem. Soc.* **2012**, *134*, 14033.
(34) Makongo, J. P. A.; Misra, D. K.; Zhou, X. Y.; Pant, A.; Shabetai, M. R.; Su, X. L.; Uher, C.; Stokes, K. L.; Poudeu, P. F. P. *J. Am. Chem. Soc.* **2011**, *133*, 18843.
(35) Makongo, J. P. A.; Misra, D. K.; Salvador, J. R.; Takas, N. J.; Wang, G. Y.; Shabetai, M. R.; Pant, A.; Paudel, P.; Uher, C.; Stokes, K. L.; Poudeu, P. F. P. *J. Solid State Chem.* **2011**, *184*, 2948.
(36) Misra, D. K.; Makongo, J. P. A.; Sahoo, P.; Shabetai, M. R.; Paudel, P.; Stokes, K. L.; Poudeu, P. F. P. *Sci. Adv. Mater.* **2011**, *3*, 607.
(37) *SHELTXL*, v6.12; Bruker Analytical X-ray Instruments, Inc.: Madison, WI, 2000.
(38) *DIAMOND*, Version 3.1a; Crystal Impact GbR: Bonn, Germany, 2005.
(39) Shannon, R. D. *Acta Crystallogr. A* **1976**, *32*, 751.
(40) Kanamori, J. *J. Phys. Chem. Solids* **1959**, *10*, 87.
(41) Goodenough, J. B. *J. Phys. Chem. Solids* **1958**, *6*, 287.
(42) Goodenough, J. B. *Phys. Rev.* **1955**, *100*, 564.
(43) Wolff, P. A.; Bhatt, R. N.; Durst, A. C. *J. Appl. Phys.* **1996**, *79*, 5196.
(44) Kaminski, A.; Das Sarma, S. *Phys. Rev. Lett.* **2002**, *88*, 247202.
(45) Sze, S. M. *Physics of Semiconductors Devices*, 2nd ed.; Wiley: Weinheim, 1981.

DOI: 10.1021/ja5084255
J. Am. Chem. Soc. 2015, 137, 691−698